Article

Real-Time Visual Sensing of Heat or Mass Transfer Processes for Microfluids via Tamm Plasmon Polaritons

Haoyue Hao and Liang Li*

ACCESS | 📊 Metrics & More | 📖 Article Recommendations

ABSTRACT: Heat or mass transfer processes of microfluids are very important in bioscience, environmental engineering, and food science, which are still hard to detect in real time. To overcome this difficulty, we try to use Tamm plasmon polaritons to enhance the interaction of light with microfluids. The main structure of the proposed configuration is Ag-photonic crystal (PhC) cavity, which can generate strong photonic localization by exciting Tamm plasmon polaritons. The results show that the enhancement of light intensity reaches ∼90 times in the cavity and the reflectance spectrum of the proposed structure exists in a narrow valley near 632.8 nm. This illustrates the generation of Tamm plasmon polaritons in the proposed structure. By injecting the microfluids into the cavity, the heat and mass transfer processes of the microfluids will have considerable influence on the reflectance of the proposed structure. Simulation results show that the concentration or temperature distributions of the microfluids can be effectively detected by analyzing the brightness of the imaging pictures, which is real-time and visible. Meanwhile, the sensitivity of the proposed configuration can be tuned by setting proper base parameters. This proposed configuration will have great potential in the study of microfluids, especially for the dynamic processes.
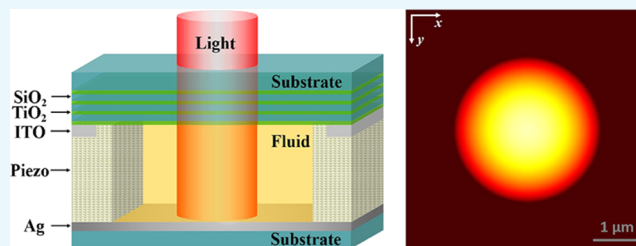
INTRODUCTION

Tamm plasmon polaritons (TPPs) traditionally formed near the interface between the photonic crystal (PhC) and the metal film can be excited with both transverse electric (TE) and transverse magnetic (TM) polarized lights without the assistance of external structures.[1,2] Meanwhile, TPPs can selectively transform the energy of specific wavelength light into an electromagnetic mode and generate optical field enhancement. The easy excitation mode and high optical field localization make TPPs attractive for many kinds of fields, such as optical sensors,[3−6] single photon source,[7] confined laser,[8,9] nonlinear optical effects,[10,11] perfect absorption,[12,13] and tunable filters.[14,15] Benefiting from the increasingly mature preparation technology, TPPs are experimentally studied and plenty of results match well with theoretical studies, which demonstrates its valid value and great potential.[16−20] Comparing with the traditional TPPs generated near the interface,[21−25] multiple TPPs are found in cavities by increasing the thickness of the top layer in the photonic crystal.[14,26,27] Recently, TPPs generated by a metal-PhC cavity are demonstrated in the visible band, which highly increases the application of TPPs, especially in the optical sensors.[28] However, the metal-PhC cavity reported is several decades nanometers, which limits the size of the detection object. In this work, we design a metal-PhC microcavity that could generate multiple TPPs. This structure is more suitable for the detection of microsize materials, such as biological tissues and microfluids. Meanwhile, the optical properties of this metal-

PhC microcavity are better than the reported nanocavity, which can increase the sensitivity of detection.

Explorations are increasingly evolving to smaller scale and size, which makes microfluids more important in modern science and technology, such as bioscience,[29,30] environmental engineering,[31] food science,[32,33] and optofluidics.[34] Heat and mass transfer characteristics of microfluids are supertiny processes that are hard to be real-time observed. An effective method to instantaneously detect the heat and mass transfer processes is urgently necessary for microfluids. Thus, we design a configuration that could real-time image the concentration or temperature distributions of microfluids. This proposed configuration may play an important role in the study of heat and mass transfer processes.

STRUCTURE AND METHODS

The main body of the Ag-PhC cavity consists of the Ag film, microcavity, PhC, piezoelectric film, and ITO film, as shown in Figure 1. The PhC consists of three layers of SiO$_2$ (with a thickness of 100 nm) and four layers of TiO$_2$ (with a thickness
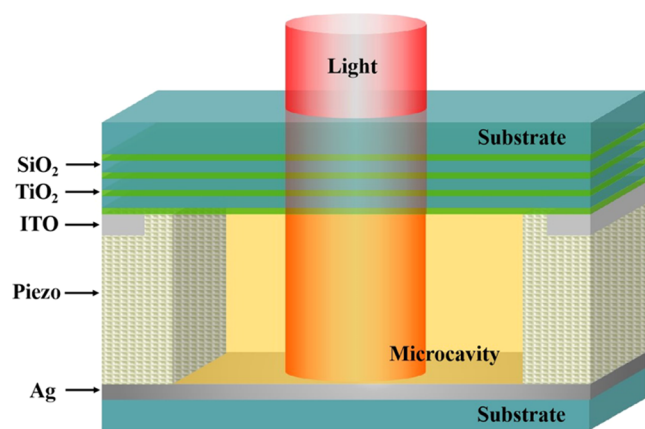
Figure 1. Schematic of the Ag-PhC microcavity structure.

of 60 nm). The layer number of the PhC is optimized such that the proposed configuration can have higher sensitivity. The influence of the layer number on TPPs is complicated and has been discussed in ref 28. To simplify the discussion, the optimized result is directly used in the proposed structure and the detailed optimizing process is not shown in this work. The thickness of the Ag film is 200 nm, which can ensure zero optical transmittance of the structure. The piezoelectric film, ITO film, and microcavity are inserted between the PhC and the Ag film. The thickness of the piezoelectric film and ITO film is ~3.07 μm. The piezoelectric film could be used to accurately control the distance between the Ag film and the PhC (or the thickness of the microcavity). The ITO and Ag films can work as two electrodes to adjust the piezoelectric film. Here, we discuss the preparation process of this proposed structure. First, we prepare the Ag film and PhC on silica substrates. Second, we prepare ITO and piezoelectric films on the PhC. Then, we etch a channel on the piezoelectric and ITO films. Finally, we attach the piezoelectric film on the Ag film.

The reflectance and absorptance spectra of the proposed structure can be theoretically investigated by the transfer matrix approach. There are two different matrices in this method: the transmission matrix (M_T) and the propagation matrix (M_P), which can be described as

$$M_{Tk} = \frac{1}{t_k}\begin{bmatrix} 1 & r_k \\ r_k & 1 \end{bmatrix}, \quad M_{Pk} = \begin{bmatrix} \exp(-i\varphi_k) & 0 \\ 0 & \exp(-i\varphi_k) \end{bmatrix} \quad (1)$$

where t_k and r_k are the transmission and reflection coefficients of light transmission from the $(k - 1)$th layer to the kth layer, which can be derived from the Fresnel formula. φ_k is the phase of light propagating in the kth layer. The total transfer matrix of the structure can be deduced as

$$M = M_{T1}M_{P1}M_{T2}M_{P2}\cdots M_{TM}M_{PM}M_{TA}M_{PA} \quad (2)$$

where M_{TM} is the transmission matrix for the interface of the TiO$_2$ layer and the microcavity, M_{PM} is the propagation matrix of the microcavity, M_{TA} is the transfer matrix for the interface of the microcavity and Ag film, and M_{PA} is the propagation matrix of the Ag film. Then, the reflectance and absorptance of the structure can be expressed as

$$R = \left|\frac{M_{21}}{M_{11}}\right|^2, \quad A = 1 - R \quad (3)$$

. The reflectance and absorptance spectra of the proposed structure are shown in Figure 2a. It can be seen that several
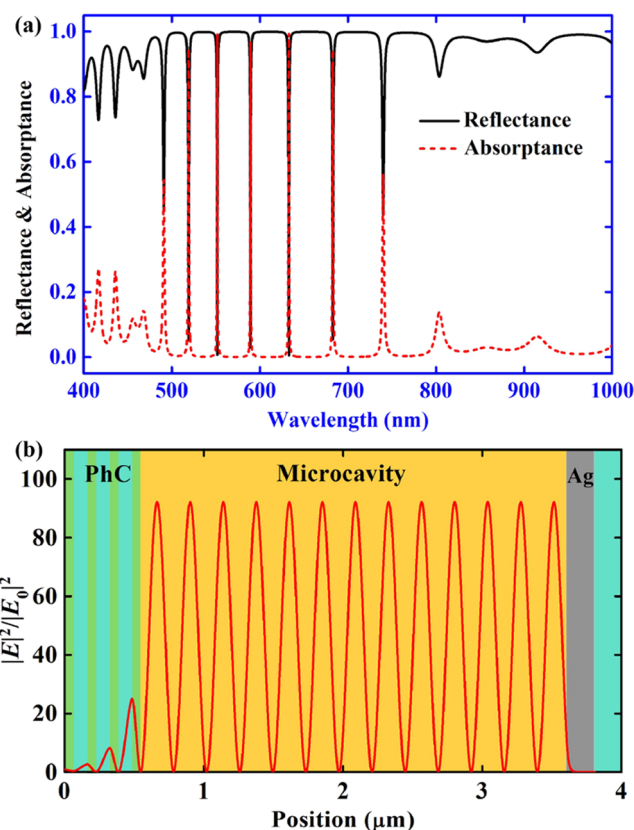
Figure 2. (a) Reflectance and absorptance spectra of the Ag-PhC microcavity. (b) Normalized electric field distribution of the Ag-PhC microcavity at 632.8 nm.

narrow absorption peaks appear in the stop-band of the PhC, which means the structure has multiple channels to generate Tamm plasmon polaritons. Focusing on the narrow absorption peak near 632.8 nm, the reflectance spectrum shows a narrow valley at the corresponding wavelength. The full width at half-maximum (FWHM) of this absorption peak is ~0.62 nm. To analyze the optical field distribution of the proposed structure, the normalized electric field distribution is derived at 632.8 nm, as shown in Figure 2b. It can be found that high photonic localization is generated in the microcavity. The localization exists at 13 positions and the enhancement of light intensity reaches ~90 times. The enhancement of light intensity is also higher than the reported results. In addition, this structure nearly reaches perfect absorption at 632.8 nm. These results show that strong TPPs are generated in the Ag-PhC microcavity. The refractive indices of SiO$_2$ and TiO$_2$ layers are 1.45 and 2.58, respectively. The refractive index of the microcavity is set as 1.33 (RI for pure water at 300 K). The distance between the Ag film and the PhC is adjusted to 3.067 μm.

■ RESULTS AND DISCUSSION

Excitation of TP Modes. In this paper, the phase matching condition of TP mode can be deduced as[2]

$$r_{BR}r_S \exp(2i\varphi_i) = 1 \quad (4)$$

where r_{BR} is the reflection coefficient of the light incident from the microcavity to the Bragg mirror and r_S is the reflection coefficient of the light incident from the microcavity to the silver film. i is the imaginary unit and $\varphi_i = 2\pi n_i d_i / \lambda$ is the phase of light propagating in the microcavity. We can rewrite eq 4 in the form

$$\varphi_i + \varphi_r = 2m\pi \quad (m = 0, 1, 2, ...) \tag{5}$$

where φ_r is the phase variation induced by the reflection on the Bragg mirror and the silver film. From eq 5, we can obtain that Tamm plasmon polaritons can be excited in different orders (with different m). In Figure 2a, we can find that seven narrow absorption peaks are generated in the stop-band of the PhC. These seven absorption peaks originate from the energy coupling of different order TPPs. The order numbers (m) of these absorption peaks are 9, 10, 11, 12, 13, 14, and 15 from short to long wavelength, sequentially. Especially, the order number (m) of the absorption peak near 632.8 nm is 13, which corresponds to the electric field distribution in Figure 2b.

Response on the Phase Variation. In the Ag-PhC microcavity, strong enhancement of the optical field is generated. If we inject the microfluids into this microcavity, the microfluids will have a strong interaction with light. Thus, the optical properties of the proposed structure will highly depend on the refractive index of microfluids. Since heat and mass transfer processes will influence the refractive index of microfluids, the proposed structure can realize the sensing of these two processes. The phase of the microcavity can be described as

$$\varphi_M = 2\pi \frac{n_M d_M}{\lambda} \tag{6}$$

where n_M and d_M are the refractive index and thickness of the microfluid. λ is the wavelength of light. The phase response for the microcavity is shown in Figure 3a. As shown by the solid line, the reflectance of the proposed structure is near zero
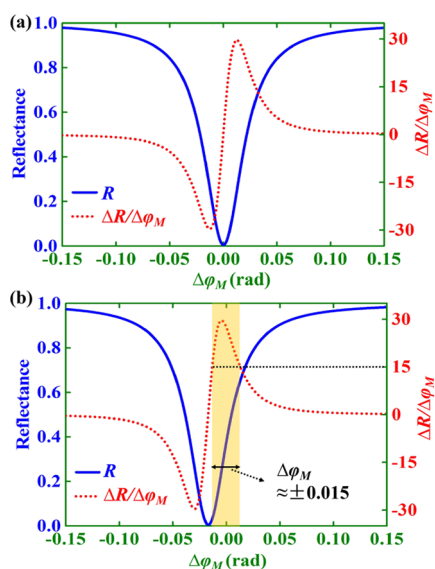
Figure 3. (a) Reflectance and the derivative of reflectance as a function of $\Delta\varphi_M$ at 632.8 nm. (b) Reflectance and the derivative of reflectance as a function of $\Delta\varphi_F$ at 632.8 nm when d_c is 1.2 nm thicker than the original structure. $\Delta\varphi_M$ is the phase variation of the microcavity.

when φ_M is at the origin and dramatically increases when φ_M becomes larger or smaller. The maximum rate of reflectance change reaches 30 per radian near ± 0.015 rad, as illustrated by the dotted line.

The best phase response position does not exist near the origin, and reflectance change is near zero when $\Delta\varphi_F = 0$. This is not suitable for the detection of supertiny variation of φ_F. To overcome this defect, we slightly adjust the thickness of the microcavity (d_m) by tuning the applied voltage of the piezoelectric film. As shown in Figure 3b, zero point of reflectance shifts to $\Delta\varphi_F \approx -0.015$ rad and the best phase response position shifts to the origin. The thickness of the cavity is 1.2 nm thicker than the original structure. The reflectance rate of change can stay above 15 per radian in the range of -0.015 to $+0.015$ rad that can highly enhance the application value of the proposed structure in the sensing of the microcavity.

Schematic of the Proposed Configuration. The proposed imaging configuration mainly consists of the laser source (632.8 nm), bean expander, beam splitter (45 deg), attenuator, microscope, and charge coupled device (CCD) camera, as shown in Figure 4. The microcavity works as a fluid
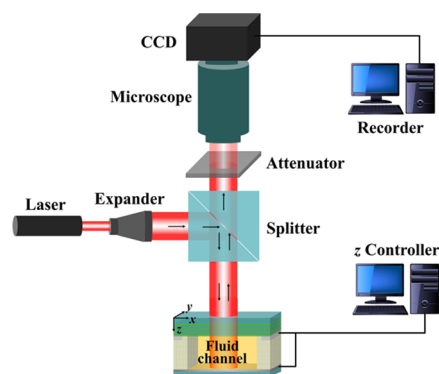
Figure 4. Schematic of the proposed configuration for imaging micro-nanofluids.

channel. First, incident laser is expanded, shaped, and split. The reflection part of the split laser vertically passes the PhC and the fluid to the Ag film. Then, the reflection laser from the Ag-PhC microcavity is split into the transmission part and reflection part in the splitter. This transmission part will be attenuated and detected with a microscope. At last, the image of the microfluids will be recorded with a CCD camera. In addition, the distance between the PhC and the Ag film can be accurately adjusted by tuning the applied voltage on the piezoelectric film.

This configuration is based on an optical system, which means it has a high time response on the detection of the microfluid. The maximum limitation on the time response is the recording speed of the CCD camera. With the development of optical and electrical technology, the response time of the high-speed CCD camera can reach several microseconds. Thus, the response time of this configuration can reach microsecond levels, which can be called as real-time recording in this situation. In addition, the intensity of the detected light that is highly weaker than the influence of light on the microfluids can be neglected.

Simulation of Mass Sensing. Molecular diffusion is an important process for microfluids, especially in the analysis of mass transfer and exchange. To clearly demonstrate the
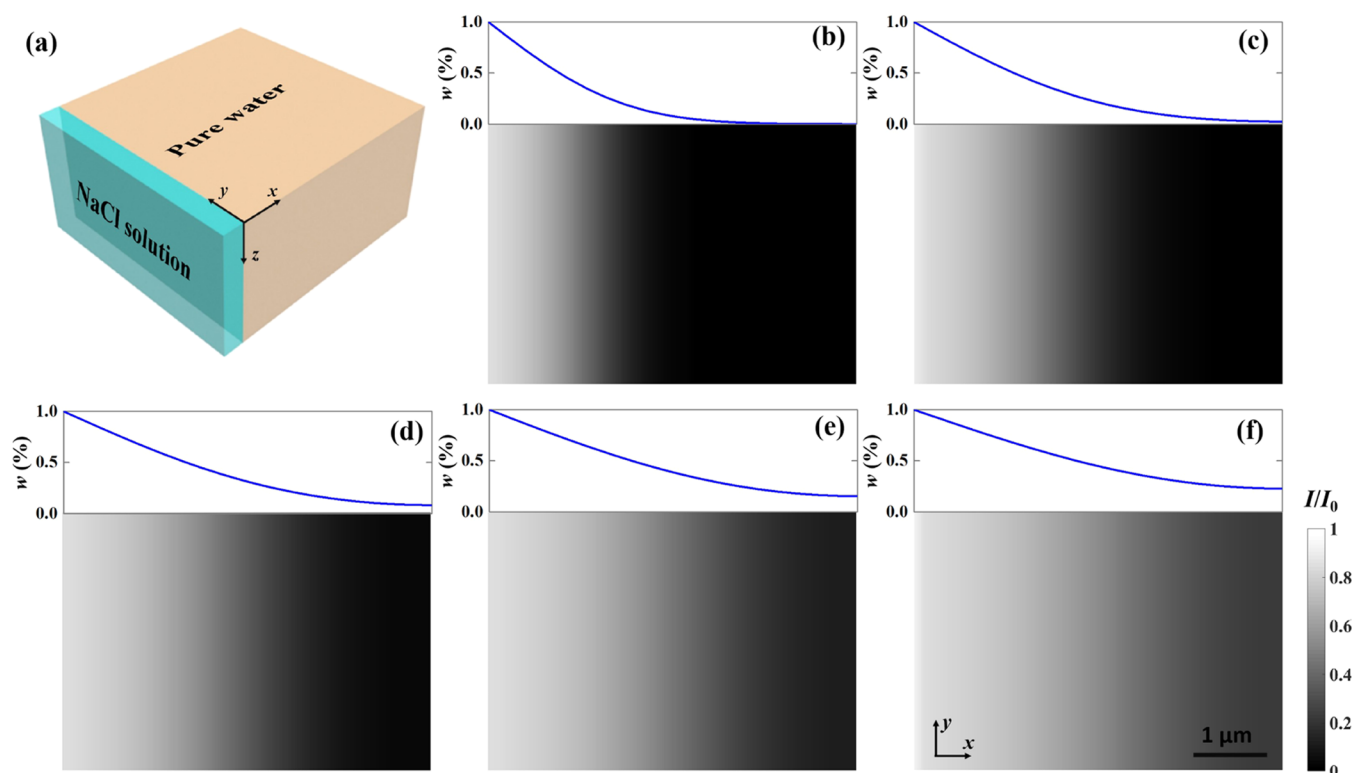
Figure 5. (a) Schematic of concentration distribution for NaCl solution when t = 0 ms. Imaging pictures of concentration distribution for NaCl solution when (b) t = 1 ms, (c) t = 2 ms, (d) t = 3 ms, (e) t = 4 ms, and (f) t = 5 ms.
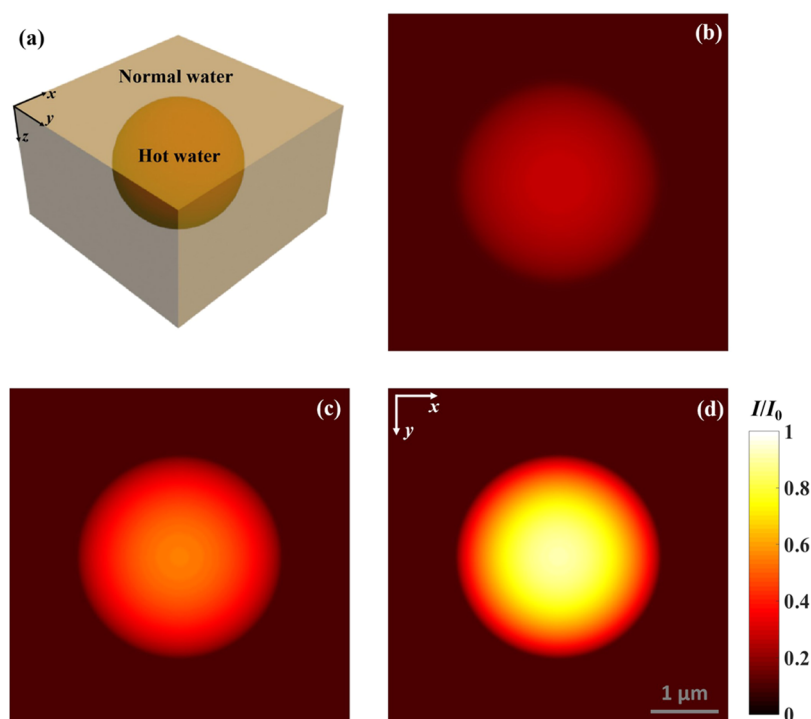
Figure 6. (a) Schematic of temperature variation for pure water. Imaging pictures of temperature variation for (b) ΔT = 0.5 K, (c) ΔT = 1.0 K, and (d) ΔT = 1.5 K.

imaging quality of the proposed configuration for concentration distribution, the diffusion of NaCl solution is investigated. The simulation results are calculated with the transfer matrix approach. To simplify the discussion, basic approximations are used: scattering and refraction are

neglected in the microfluids since their refractive index variation is supertiny (on the order of 10^{-4}). Figure 5a shows the initial concentration distribution of the NaCl solution. The fluid in the channel is pure water and NaCl solution exists at the boundary of the fluid channel. The mass

concentration of NaCl solution is 1 wt %. Hence, the phase variation of microfluids can be deduced as

$$\Delta \varphi_F = 2\pi \frac{d_F}{\lambda} \Delta n_F \tag{7}$$

Here, Δn_F is the variation of the refractive index for the fluid channel and Δn_F is appropriately proportional to the variation of mass concentration for NaCl, which can be described as Δn_F = 0.174 × Δw at room temperature.[35] Thus, the mass concentration of NaCl solution can be represented by the phase variation, which is related to the reflectance of the proposed structure. By detecting the reflected light from the proposed structure, the mass concentration can be derived in the imaging pictures. Figure 5b−f shows the real-time imaging picture of the fluid channel. Subgraphs show the mass concentration of NaCl at the corresponding position. The brightness of the imaging pictures is normalized by the light intensity of 1 wt % NaCl solution. The lowest brightness is set as 0 wt % NaCl solution (pure water). Then, the real-time concentration distribution can be obtained from the imaging pictures along with analyzing the brightness distribution. It can be seen that the brightness of each position increases with the increase in mass concentration. And the brightness contrast becomes higher when the concentration variation increases. This satisfies the need of real-time imaging for concentration distribution. However, the relation between the concentration and the brightness is nonlinear. This means that a proper correspondence relation should be built before sensing. The sensitivity of concentration can be estimated with the sensitivity of the CCD camera. The detection precision for light intensity can reach a thousandth of the detection range for CCD cameras. This means that the detection precision for reflectance variation can reach 5 × 10⁻⁴ if the base reflectance is set as 0.5. From Figure 3, the reflectance rate of change can easily stay above 15 per radian. Thus, the detection precision for phase variation can reach ∼3 × 10⁻⁵ rad. Combined with eq 7, the sensitivity of concentration detection can be roughly estimated at 0.001 wt %. Meanwhile, this sensitivity can be increased by tuning the base concentration (corresponding to the lowest brightness). The base concentration can be adjusted by tuning the applied voltage on the piezoelectric film, which will shift the position of zero reflectance point by changing the d_F.

Simulation of Heat Sensing. Detection of temperature variation is an important method to study the heat transfer process. The detection of the temperature variation of a spherical area by the proposed configuration is investigated, as shown in Figure 6. This study is based on pure water and the normal water is set at 300 K. There is a spherical area with a diameter of 3 μm that has a different temperature than the normal water. The dependence of refractive index on temperature for pure water can be described as[36]

$$\frac{n_F^2 - 1}{n_F^2 + 2} = c_T T' + C_{\rho,\lambda} \tag{8}$$

where T' is the normalized temperature and $T' = T/273.15$ K. T is the absolute temperature of pure water. c_T is the coefficient of temperature. $C_{\rho,\lambda}$ is a constant that relates to density and wavelength. And $c_T = -3.334 \times 10^{-3}$ K⁻¹, $C_{\rho,\lambda}$ = 0.2091 when the density of pure water and the light wavelength are 1000 kg·m⁻³ and 632.8 nm, respectively. Similarly, the temperature also can be represented by the phase

variation that can be derived in the imaging pictures. Since the brightness of the imaging pictures corresponds to the phase variation, the temperature variation can be visually analyzed by the brightness of each position, as shown in Figure 6b−d. It can be found that the brightness of the circular region, corresponding to the hot water sphere, increases with the increase in temperature variation. The temperature variation of the three pictures can be easily distinguished from the brightness. As discussed above, the detection precision for phase variation has been estimated at ∼3 × 10⁻⁵ rad. Combined with eq 8, the sensitivity of temperature variation can be roughly estimated at 0.1 K. The sensitivity of the thermal imagers can reach ∼0.1 K, which is on the same level with the proposed configuration. However, thermal imagers are traditionally for large-sized objects that are hard to realize the detection of microsize objects, such as microfluids.

However, the brightest position is at the center of the circular region and gets gradually darker outward to the edge. The appearance comes from the shape of the temperature variation region, which cannot be distinguished from the absolute temperature variation. To overcome this difficulty, the detection region needs to be imaged from different observation angles. Nevertheless, the proposed configuration can also realize the visual imaging for specific objects with known shapes.

From the above results, we can find that both concentration and temperature distributions have an influence on the brightness of the imaging pictures. Thus, the brightness variation of the imaging picture cannot be clearly distinguished into the concentration or temperature variation. Therefore, mass transfer and heat transfer processes cannot be simultaneously detected for this configuration. Although the proposed configuration has this limitation, it still has practical values in the situations that have a low temperature variation or have related homogeneous solution. Actually, these situations are normal in practice, such as diffusion and drift of ions, low thermal reaction, and chemical and physical processes of particles in solution. In addition, the evolution of concentration can be extracted if the influence of temperature is removed with the assistance of the thermal imaging equipment.

Tuning of Base Brightness. In practice, we need to detect different microfluids with different concentration or temperature ranges. To ensure the high sensitivity for these different microfluids, the base brightness of imaging pictures needs to be set at a proper position. This setting can be realized by tuning the thickness of the microcavity (d_c) by adjusting the applied voltage of the piezoelectric film. The tuning of d_c for different concentration or temperature ranges was investigated, as shown in Figure 7. It can be seen that the tuning of d_c is in proportion to the base concentration or temperature. The variation of d_c for the concentration of NaCl solution is ∼−4.0 nm per 1 wt %. The variation of d_c for the temperature is ∼0.05 nm/degree.

■ CONCLUSIONS

In summary, TPPs are generated in a Ag-PhC microcavity, which shows excellent optical properties. Based on the Ag-PhC microcavity, an effective configuration to image the heat or mass transfer processes of microfluids is revealed. The simulation for the imaging of concentration and temperature distributions shows great results. By analyzing the brightness, the concentration or temperature distributions can be presented separately in the imaging pictures. The sensitivity
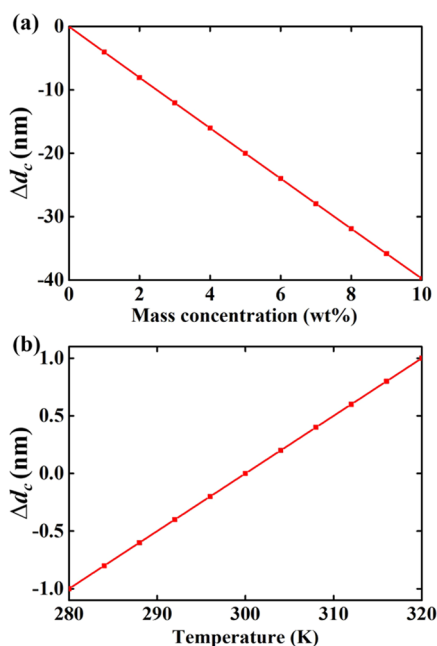
Figure 7. Relationships between thickness variation of d_c and (a) base concentration and (b) base temperature.

for the concentration and temperature sensing can reach 0.001 wt % and 0.1 K, respectively. Based on TPPs, the proposed configuration enhances the interaction of light with microfluids and then realizes the optical sensing of heat or mass transfer processes. This method is novel and unique, which is excellent in the response speed, spatial continuity, micromation of size, and visual presentation. The proposed structure cannot be perfectly prepared using the current preparation technology of films. With the rapid development of preparation technology, we believe the proposed configuration will play an important part in the near future.

■ AUTHOR INFORMATION

Corresponding Author

Liang Li − *School of Physics and Optoelectronic Engineering, Shandong University of Technology, Zibo 255000, China;* ⊙ orcid.org/0000-0003-0270-8080; Email: liangli@ sdut.edu.cn

Author

Haoyue Hao − *School of Physics and Optoelectronic Engineering, Shandong University of Technology, Zibo 255000, China*

Complete contact information is available at:
https://pubs.acs.org/10.1021/acsomega.2c02481

Notes

The authors declare no competing financial interest.

■ REFERENCES

(1) Malkova, N.; Ning, C. Z. Shockley and Tamm surface states in photonic crystals. *Phys. Rev. B* **2006**, *73*, No. 113113.

(2) Sasin, M. E.; Seisyan, R. P.; Kalitteevski, M. A.; Brand, S.; Abram, R. A.; Chamberlain, J. M.; Egorov, A. Yu.; Vasilev, A. P.; Mikhrin, V. S.; Kavokin, A. V. Tamm plasmon polaritons: Slow and spatially compact light. *Appl. Phys. Lett.* **2008**, *92*, No. 251112.

(3) Zhang, W. L.; Wang, F.; Rao, Y.; Jiang, Y. Novel sensing concept based on optical Tamm plasmon. *Opt. Express* **2014**, *22*, 14524−14529.

(4) Zhang, C.; Wu, K.; Giannini, V.; Li, X. Planar hot-electron photodetection with Tamm plasmons. *ACS Nano* **2017**, *11*, 1719−1727.

(5) Li, N.; Tang, T.; Li, J.; Luo, L.; Sun, P.; Yao, J. High sensitive sensors of fluid detection based on magneto-optical optical Tamm state. *Sens. Actuators, B* **2018**, *265*, 644−651.

(6) Zhu, Y.; Yu, P.; Liu, T.; Xu, H.; Govorov, A. O.; Wang, Z. Nanolayered Tamm plasmon-based multicolor hot electron photodetection for O- and C-band telecommunication. *ACS Appl. Electron. Mater.* **2021**, *3*, 639−650.

(7) Gazzano, O.; Vasconcellos, S. M.; Gauthron, K.; Symonds, C.; Voisin, P.; Bellessa, J.; Lemaitre, A.; Senellart, P. Single photon source using confined Tamm plasmon modes. *Appl. Phys. Lett.* **2012**, *100*, No. 232111.

(8) Symonds, C.; Lheureux, G.; Hugonin, J. P.; Greffet, J. J.; Laverdant, J.; Brucoli, G.; Lemaitre, A.; Senellart, P.; Bellessa, J. Confined Tamm plasmon lasers. *Nano Lett.* **2013**, *13*, 3179−3184.

(9) Toanen, V.; Symonds, C.; Benoit, J. M.; Gassenq, A.; Lemaitre, A.; Bellessa, J. Room-temperature lasing in a low-loss Tamm plasmon cavity. *ACS Photonics* **2020**, *7*, 2952−2957.

(10) Lee, K. J.; Wu, J. W.; Kim, K. Enhanced nonlinear optical effects due to the excitation of optical Tamm plasmon polaritons in one-dimensional photonic crystal structures. *Opt. Express* **2013**, *21*, 28817−28823.

(11) Xue, C.-h.; Jiang, H.; Lu, H.; Du, G.; Chen, H. Efficient third-harmonic generation based on Tamm plasmon polaritons. *Opt. Lett.* **2013**, *38*, 959−961.

(12) Gong, Y.; Liu, X.; Lu, H.; Wang, L.; Wang, G. Perfect absorber supported by optical Tamm states in plasmonic waveguide. *Opt. Express* **2011**, *19*, 18393−18398.

(13) Li, L.; Zhao, H.; Zhang, J. Tunable perfect absorber supported by accumulation electron gas at ITO-dielectric heterointerface. *J. Phys. D: Appl. Phys.* **2017**, *50*, No. 405109.

(14) Wang, X.; Jiang, X.; You, Q.; Guo, J.; Dai, X.; Xiang, Y. Tunable and multichannel terahertz perfect absorber due to Tamm surface plasmons with graphene. *Photonics Res.* **2017**, *5*, 536−542.

(15) Li, L.; Zhao, H.; Zhang, J. Electrically tuning reflection of graphene-based Tamm plasmon polariton structures at 1550 nm. *Appl. Phys. Lett.* **2017**, *111*, No. 083504.

(16) Yang, Z.-Y.; Ishii, S.; Yokoyama, T.; Dao, T. D.; Sun, M.; Pankin, P. S.; Timofeev, I. V.; Nagao, T.; Chen, K. Narrowband wavelength selective thermal emitters by confined Tamm plasmon polaritons. *ACS Photonics* **2017**, *4*, 2212−2219.

(17) Mischok, A.; Siegmund, B.; Ghosh, D. S.; Benduhn, J.; Spoltore, D.; Bohm, M.; Frob, H.; Korner, C.; Leo, K.; Vandewal, K. Controlling Tamm plasmons for organic narrowband near-infrared photodetectors. *ACS Photonics* **2017**, *4*, 2228−2234.

(18) Tsurimaki, Y.; Tong, J. K.; Boriskin, V. N.; Semenov, A.; Ayzatsky, M. I.; Machekhin, Y. P.; Chen, G.; Boriskina, S. V. Topological engineering of interfacial optical Tamm states for highly sensitive near-singular-phase optical detection. *ACS Photonics* **2018**, *5*, 929−938.

(19) Cheng, H.-C.; Kuo, C.; Hung, Y.; Chen, K.; Jeng, S. Liquid-crystal active Tamm-plasmon devices. *Phys. Rev. Appl.* **2018**, *9*, No. 064034.

(20) Afinogenov, B. I.; Bessonov, V. O.; Soboleva, I. V.; Fedyanin, A. A. Ultrafast all-optical light control with Tamm plasmons in photonic nanostructures. *ACS Photonics* **2019**, *6*, 844−850.

(21) Braun, T.; Baumann, V.; Iff, O.; Hofling, S.; Schneider, C.; Kamp, M. Enhanced single photon emission from positioned InP/GaInP quantum dot coupled to a confined Tamm-plasmon mode. *Appl. Phys. Lett.* **2015**, *106*, No. 041113.

(22) Das, R.; Srivastava, T.; Jha, R. On the performance of Tamm-plasmon and surface-plasmon hybrid-mode refractive-dindex sensor in metallo- dielectric heterostructure configuration. *Sens. Actuators, B* **2015**, *206*, 443−448.

(23) Lundt, N.; Klembt, S.; Cherotchenko, E.; Betzold, S.; Iff, O.; Nalitov, A. V.; Klaas, M.; Dietrich, C. P.; Kavokin, A. V.; Hofling, S.; Schneider, C. Room-temperature Tamm-plasmon exciton-polaritons with a WSe_2 monolayer. *Nat. Commun.* **2016**, *7*, No. 13328.

(24) Zhang, C.; Wu, K.; Giannini, V.; Li, X. Planar hot-electron photodetection with Tamm plasmons. *ACS Nano* **2017**, *11*, 1719−1727.

(25) Paulauskas, A.; Tumenas, S.; Selskis, A.; Tolenis, T.; Valavicius, A.; Balevicius, Z. Hybrid Tamm-surface plasmon polaritons mode for detection of mercury adsorption on 1D photonic crystal/gold nanostructures by total internal reflection ellipsometry. *Opt. Express* **2018**, *26*, 30400−30408.

(26) Zhou, H.; Yang, G.; Wang, K.; Long, H.; Lu, P. Multiple optical Tamm states at a metal-dielectric mirror interface. *Opt. Lett.* **2010**, *35*, 4112−4114.

(27) Fei, Y.; Liu, Y.; Dong, D.; Gao, K.; Ren, S.; Fan, Y. Multiple adjustable optical Tamm states in one-dimensional photonic quasicrystals with predesigned bandgaps. *Opt. Express* **2018**, *26*, 34872−34879.

(28) Li, L.; Zhao, H.; Zhang, J.; Hao, H.; Xing, F. Tunable Tamm plasmon polaritons and perfect absorption in a metal-PC cavity. *J. Phys. D: Appl. Phys.* **2019**, *52*, No. 255105.

(29) Wang, H.; Zhao, Z.; Liu, Y.; Shao, C.; Bian, F.; Zhao, Y. Biomimetic enzyme cascade reaction system in microfluidic electro-spray microcapsules. *Sci. Adv.* **2018**, *4*, No. eaat2816.

(30) Sun, H.; Zheng, H.; Tang, Q.; Dong, Y.; Qu, F.; Wang, Y.; Yang, G.; Meng, T. Monodisperse alginate microcapsules with spatially confined bioactive molocules via microfluid-generated W/W/O emulsions. *ACS Appl. Mater. Interfaces* **2019**, *11*, 37313−37321.

(31) Ottesen, E. A.; Hong, J. W.; Quake, S. R.; Leadbetter, J. R. Microfluidic digital PCR enables multigene analysis of individual environmental bacteria. *Science* **2006**, *314*, 1464−1467.

(32) Gunes, D. Z. Microfluidics for food science and engineering. *Curr. Opin. Food Sci.* **2018**, *21*, 57−65.

(33) Wu, C.; Gao, G.; Zhai, K.; Xu, L.; Zhang, D. A visual Hg^{2+} detection strategy based on distance as readout by G-quadruplex DNAzyme on microfluidic paper. *Food Chem.* **2020**, *331*, No. 127208.

(34) Ma, C.; Yu, P.; Wang, W.; Zhu, Y.; Lin, F.; Wang, J.; Jing, Z.; Kong, X.; Li, P.; Govorov, A. O.; Liu, D.; Xu, H.; Wang, Z. Chiral optofluidics with a plasmonic metasurface using the photothermal effect. *ACS Nano* **2021**, *15*, 16357−16367.

(35) Tan, C.; Huang, Y. Dependence of refractive indies on concentration and temperature in electrolyte solution, polar solution, nanpolar solution, and protein solution. *J. Chem. Eng. Data* **2015**, *60*, 2827−2833.

(36) Schiebener, P.; Straub, J.; Levelt Sengers, J. M. H.; Gallagher, J. S. Refractive index of water and steam as function of wavelength, temperature and density. *J. Phys. Chem. Ref. Data* **1990**, *19*, 677−717.